JOURNAL OF MATERIALS SCIENCE 27 (1992) 1045–1052

SEM examination of the oxide–metal interface formed during the aqueous corrosion of a Zr–2.5 wt % Nb alloy

Y. DING, D. O. NORTHWOOD
Engineering Materials Group, University of Windsor, Windsor, Ontario, Canada N9B 3P4

The oxide–metal interface formed during the aqueous corrosion of a Zr–2.5 wt % Nb alloy has been studied by SEM, using a specimen preparation method which also has potential application to other materials containing an oxide–metal interface. The oxidation of cold-worked Zr–2.5 wt % Nb pressure tubing in pressurized lithiated water proceeds first along grain boundaries at which there is β-zirconium or its decomposition products, and then continues on the α-zirconium grains. Oxides at the oxide–metal interface formed in an aqueous environment were mainly extended along grain boundaries, and were characterized by long filaments which consisted of many fine zirconia grains. This oxidation behaviour is attributed to short-circuit diffusion at the grain boundaries which is caused by the nature of the crystallite boundaries of the oxide, the flaws arising from the oxidation of the grain boundary phases (β-Zr, its decomposition products as well as impurities), and cracking of the oxide due to phase transformations in ZrO_2. When different plane sections of the tubing are corroded, there are different corrosion rates, with the sections containing a higher area fraction of the grain boundaries with β-zirconium exhibiting higher corrosion rates. The formation of long 'fingers' of oxide made up of longer filaments of oxide, together with the higher corrosion rates in the post-transition specimens, result in the destruction of the barrier oxide layer and an increase in the oxide rate.

1. Introduction

Zirconium alloy corrosion and the associated hydrogen ingress are often considered in terms of the effects of a 'barrier layer' at the oxide–metal interface which significantly reduces hydrogen ingress, and decreases oxidation rates with time, so long as that barrier layer remains intact and protective. The oxidation kinetics of zirconium and its alloys can exhibit a transition, which is usually referred to as breakaway, from an initial period of approximately parabolic or cubic oxidation to a period of an approximately linear rate.

A number of theories and associated mechanisms have been proposed to explain the phenomenon of the breakaway. Among these theories, the micropore hypothesis [1, 2] and mechanical detachment hypothesis [3] are probably two of the most important. The micropore theory relates the breakaway in corrosion rates to the development of networks of micropores in the protective oxide film. These micropores, which were detected using a mercury porosimetry technique, were produced as a result of recrystallization of the oxide. The mechanical detachment theory attributes the breakaway in corrosion rates to an actual physical detachment of the protective oxide film. This detachment was predicted on the basis of actual stress measurements in the oxide films.

In order better to understand the corrosion and hydriding behaviour, it is important to obtain information on the nature of the oxide film, particularly that which is at or near the oxide–metal interface. There have been a limited number of electron microscopy studies of the structure of the oxide near the oxide–metal interface in corroded specimens of zirconium and its alloys [3–5]. Both TEM and SEM have been used, together with a variety of specimen-preparation methods. However, very few useful results have been obtained, primarily because of difficulties in preparing suitable specimens containing the oxide–metal interface.

In the present work, we have studied the oxide–metal interface in specimens of a Zr–2.5 wt % Nb alloy (hereafter referred to as Zr–2.5Nb) using SEM techniques. Zr–2.5Nb is used for the manufacture of nuclear-reactor pressure tubing because of its low neutron absorption cross-section, high strength and high corrosion resistance under reactor-operating conditions. The specimen preparation technique that has been developed should find application to other specimens where there is an interest in characterizing the oxide at or near the oxide–metal interface.

2. Experimental procedure

2.1. Material

The starting material was commercial grade Zr–2.5Nb alloy pressure tubing, supplied by Ontario

TABLE I Chemical analysis of Zr–2.5Nb alloy

Impurity analysis (p.p.m. by weight)													
Al	B	Cd	Co	Cr	Cu	H	Hf	Mn	Ni	Si	Ti	U	W
32	< 0.25	< 0.25	< 10	< 100	< 25	7	53	< 2.5	< 35	49	< 25	< 1.0	< 25

Element	Nb	Fe	O
Wt %	2.59	0.039	0.101

Hydro. The chemical analysis of the tubing is given in Table I. The tubing was in the cold-worked and stress-relieved (autoclaved) condition.

2.2. Corrosion tests

Specimens of approximately 20 by 10 mm by the thickness of the tubing (4 mm) were cut from the pressure tubing using a low-speed diamond saw. The specimens were then ground to remove the protective autoclave oxide film present in as-received pressure tubing and cleaned using deionized water and alcohol. The specimens were then weighed using a microbalance and size measurements were made using an optical microscope. The corrosion/hydriding tests were carried out in high-pressure (8.65 MPa), high-temperature (300 °C) static autoclaves of 50 cc capacity. Five to six specimens were put in a holder and placed in each autoclave, which was filled with 40 cc of freshly prepared LiOH solution. A LiOH concentration of 4.8 g LiOH l^{-1} deionized water was used in order to accelerate the corrosion reaction. The testing method was an interrupted one, in which one of the specimens in each autoclave was removed at fixed time intervals. When the autoclave was cooled to ambient temperature and depressurized to remove a specimen, the LiOH solution remaining was removed and replaced with fresh solution in order to ensure constancy of LiOH concentration.

2.3. Preparation of specimens for SEM examination

The specimens when removed from the autoclave had oxide on all six surfaces. The first step in specimen preparation was to cut 0.5-mm-thick sections parallel to the axial–radial and tangential–radial surfaces. This was done using a low-speed diamond saw. These sections had the thin oxide layer on one side and the metal on the other side. Fig. 1 is a schematic diagram showing how the sections were cut.

These 0.5-mm-thick cut sections were then glued, oxide side down, onto small lengths of 13-mm diameter metal rods using a thermoplastic cement (Buehler Lakeside 70). As well as securing the specimens during preparation, the metal rods acted as specimen holders for subsequent SEM examination. Aluminium or Zircaloy rod was used in the present study, but any non-magnetic metal or alloy would be satisfactory. (Magnetic materials, e.g. steel, can interfere with the imaging function of the SEM.) This operation is illustrated schematically in Fig. 2.

The metal side of the specimens was mechanically

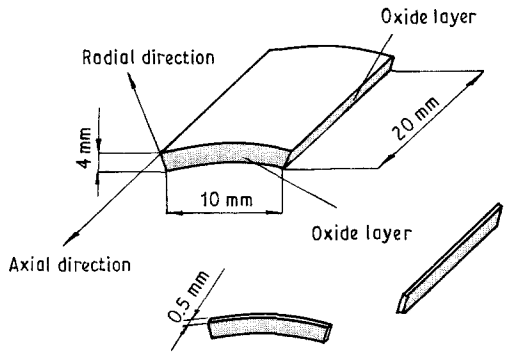

Figure 1 Sectioning of corroded specimen for subsequent SEM specimen preparation.

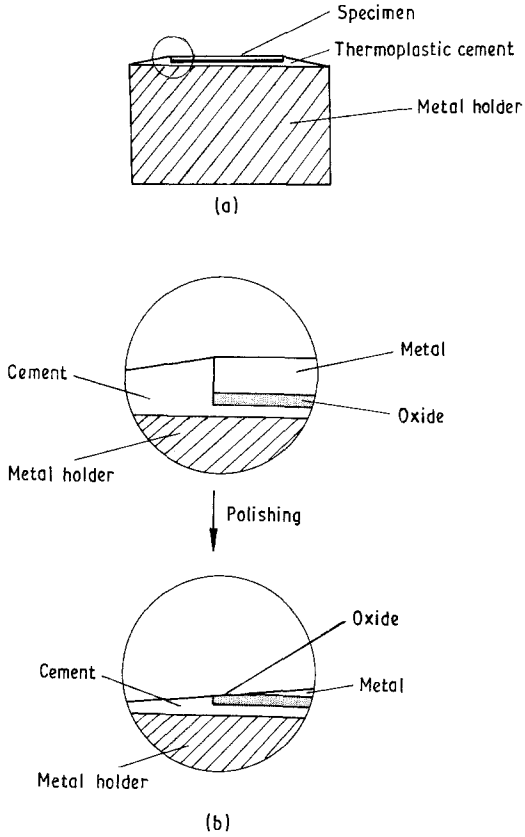

Figure 2 Schematic illustration of preparation of specimens with oxide–metal interface for SEM examination.

polished by hand until the underlying oxide layer appeared. Note that the polishing was done at an angle so that a tapered section was produced going from metal, to oxide–metal interface, to the outer oxide. Since this oxide layer is softer and more friable than the metal, the oxide–metal interface was destroyed (distorted/degraded) during this mechanical polishing operation. In order that the structure at and

near the oxide–metal interface could be better revealed, the mechanically polished specimens were chemically polished (etched) using a swabbing technique with a solution of 45 parts HNO_3:45 parts H_2O:10 parts HF. By this swab-etching technique, the metal was removed close to the oxide–metal interface. As this process was continued, more of the oxide was revealed. Before the specimens could be examined in the SEM they were coated with a thin layer (20–30 nm) of carbon using a vacuum deposition technique. This carbon layer prevents charge build-up and image degradation during SEM viewing. The SEM examination was performed using a Nanolab 7 scanning electron microscope.

3. Results

3.1. Oxidation kinetics

The corrosion behaviour of Zr–2.5Nb in a pressurized (8.65 MPa) solution of 4.8 g LiOH per litre deionized water at 300 °C is shown in Fig. 3. The data can be divided into two regimes with the initial period exhibiting parabolic kinetics and the second period having linear kinetics. From Fig. 3, we estimate that the transition in the corrosion process takes place after about 80 h of exposure to that particular environment. In order to determine the differences in the oxide microstructure, particularly the oxide at or near the oxide–metal interface (the barrier layer), between pre- and post-transition specimens, two groups of specimens were chosen, namely those exposed for 40 h (pre-transition) and 480 h (post-transition). These are shown as groups A and B in Fig. 3. By observing the differences in oxide structure, it was hoped to identify possible reasons for the transition in kinetics from parabolic to linear.

3.2. Metallography of oxides formed at grain boundaries

Fig. 4a is a SEM micrograph of an uncorroded Zr–2.5Nb pressure tubing specimen. The structure consists of long, elongated α-Zr grains with filaments of the β-Zr phase at the grain boundaries. The micrographs illustrate the relationship between the underlying metal structure and the oxidation process in Fig. 4b and c. Oxidation of cold-worked Zr–2.5Nb pressure tubing in pressurized lithiated water proceeds mainly along grain boundaries at which filaments of the β-Zr phase are present. The oxide near the oxide–metal interface, which consists of many fine zirconia grains, has formed a long filament several micrometres in length, which is consistent with length of the grain boundaries in Zr–2.5Nb specimens. Some oxide filaments were joined together to become a longer filament. Comparing Fig. 4a and c, it can be seen that the oxide filaments near the interface in a corroded specimen are wider than grain boundary regions (β-Zr phase) in an uncorroded specimen. Therefore the long oxide filaments are probably formed from oxidation of both the grain boundary phases and α-Zr grains.

All the micrographs in Fig. 4 are for sections where the oxide layer is parallel to the axial direction of the pressure tubing (i.e. axial–radial sections).

3.3. Topography of metal–oxide interface

3.3.1. Effect of orientation of specimen section

The interface topography of specimens with the oxide layer perpendicular to the axial direction of the pressure tubing (i.e. radial–tangential section) is shown in Fig. 5a and b and can be compared to the structure of the uncorroded specimen shown in Fig. 5c. Oxidation

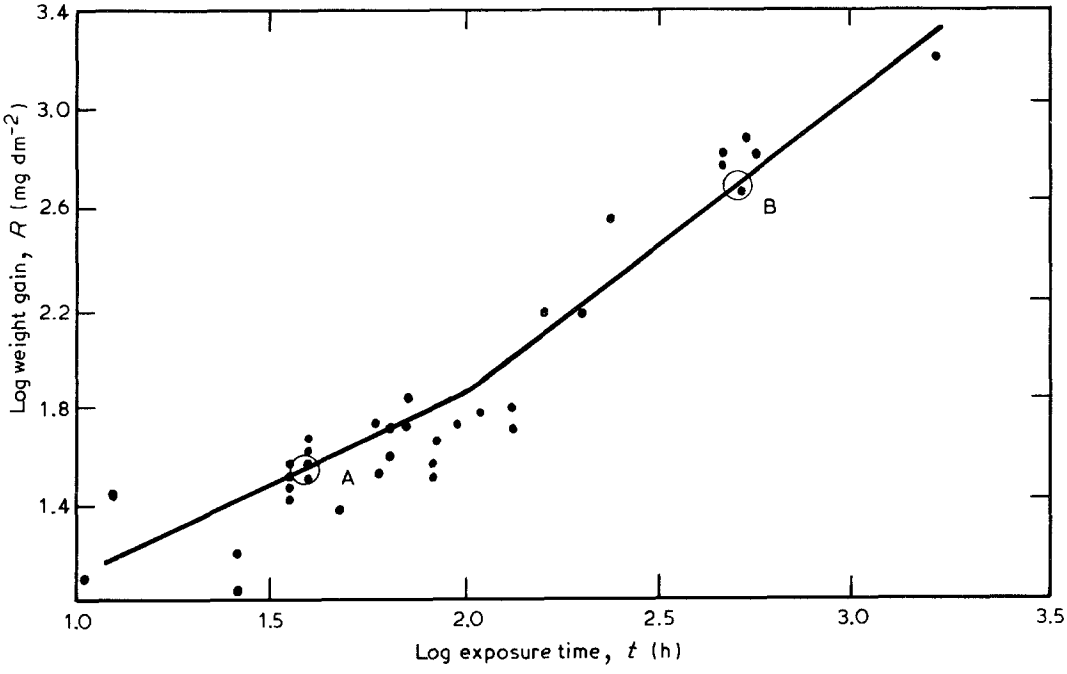

Figure 3 Oxidation kinetics for Zr–2.5 wt % Nb in 4.8 g LiOH l^{-1} deionized water at 300 °C.

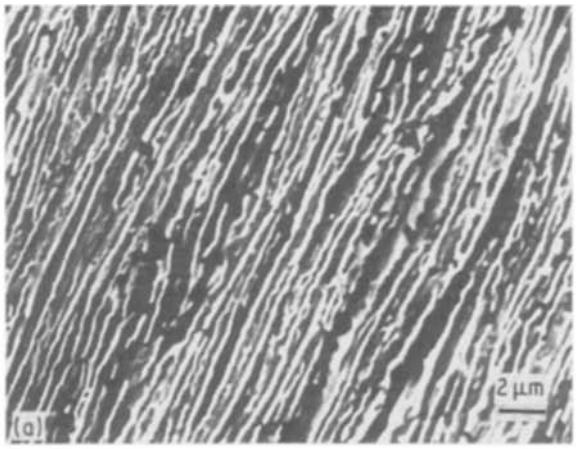

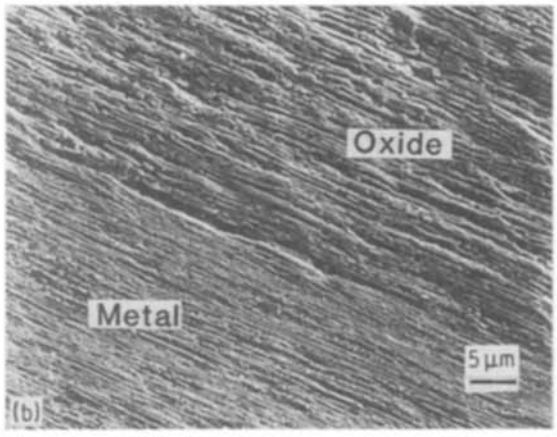

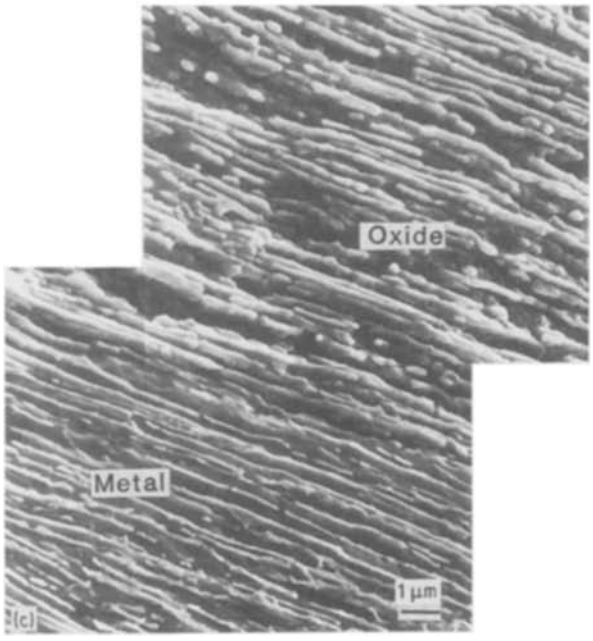

Figure 4 (a) SEM micrograph of uncorroded Zr–2.5Nb specimen (metal surface parallel to axial direction of pressure tubing). (b), (c) Topography of oxides formed at grain boundaries in pre-transition specimens (oxide layer parallel to axial direction of pressure tubing).

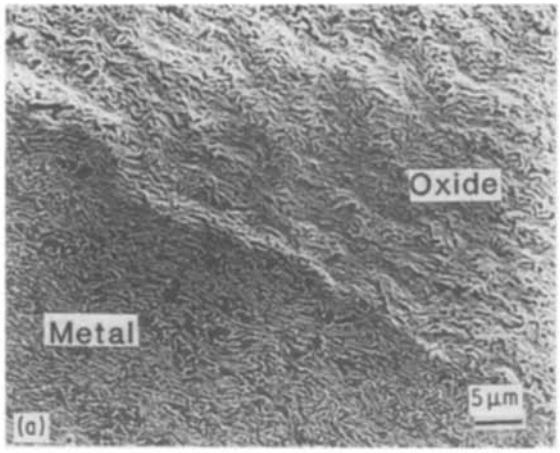

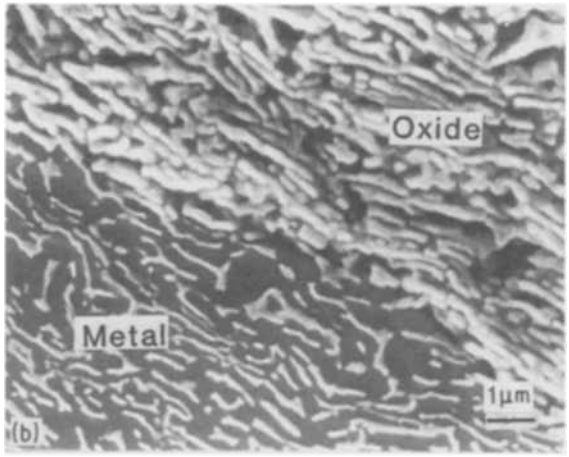

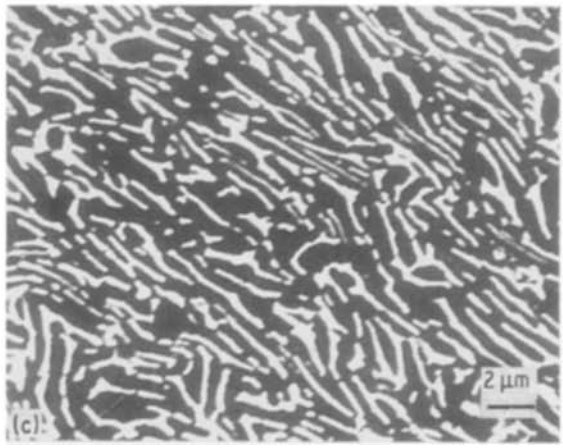

Figure 5 (a), (b) Topography of oxides formed at grain boundaries in pre-transition specimens (oxide layer perpendicular to axial direction of pressure tubing). (c) SEM micrograph of uncorroded Zr–2.5Nb specimen (metal surface perpendicular to axial direction of pressure tubing).

proceeds along grain boundaries in the same manner as in the specimens with the oxide layer parallel to axial direction of pressure tubing (see Fig. 4b and c). Because of the different α-Zr grain sizes, shapes and orientations in the different sections, these are different grain-boundary distributions on the different section faces, and corrosion can proceed at different rates. The underlying relationship between the structure of the metal and the oxidation pattern remains.

3.3.2. Effect of corrosion time

Figs 6 and 7 show the typical topographies of pre- and post-transition specimens with oxide layers parallel to

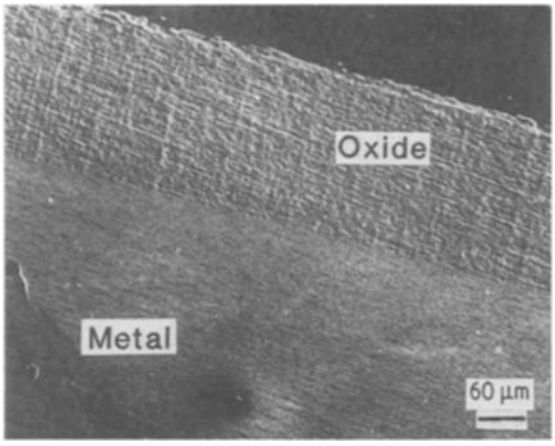

Figure 6 Micrograph of a pre-transition specimen showing uniform oxide layer parallel to axial direction of pressure tubing.

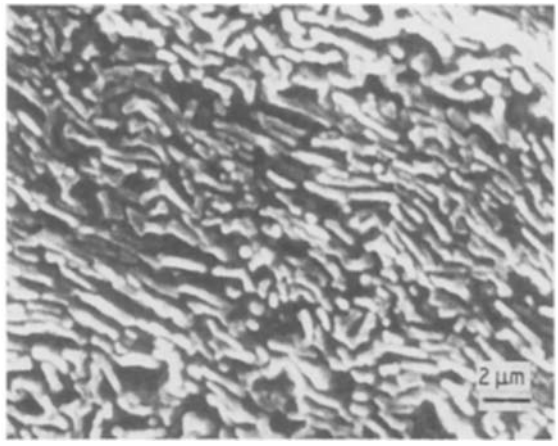

Figure 8 Oxide–metal interface in a pre-transition specimen with oxide layer perpendicular to axial direction of pressure tubing.

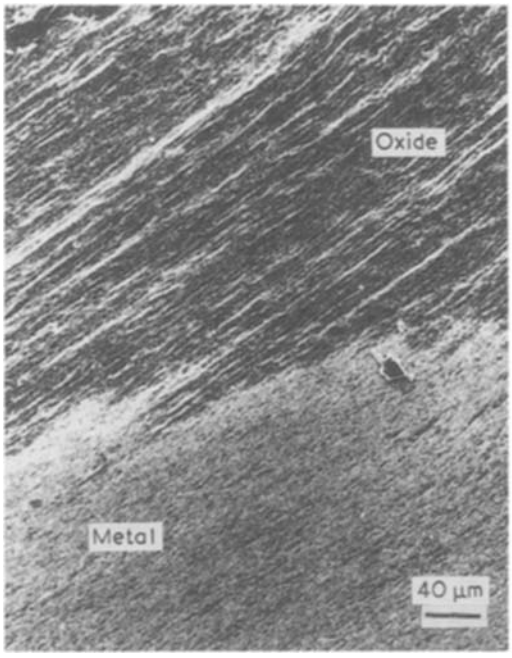

Figure 7 Micrograph of a post-transition specimen showing a non-uniform oxide layer parallel to axial direction of pressure tubing.

Figure 9 Oxide–metal interface in a post-transition specimen with oxide layer perpendicular to axial direction of pressure tubing.

the axial direction. From Figs 6 and 7 it can readily be seen that the oxide layer formed on the pre-transition specimens is characterized by a uniform thickness, and that the oxide layer formed on the post-transition specimens is not uniform. This difference is due to the fact that there were different corrosion rates at different locations in the post-transition specimens. Figs 8 and 9 show the oxide–metal interface in pre- and post-transition specimens where the oxide layers are perpendicular to axial direction. The oxides at the oxide–metal interface in pre-transition specimens form at the grain boundaries, but are wider than the original grain boundaries containing the β-Zr. Some of the oxides at the oxide–metal interface in the post-transition specimens were joined together and became long ridges, which consist of many oxide filaments where there were the highest corrosion rates. Figs 10 and 11 show the oxide–metal interface differences between pre- and post-transition specimens with oxides parallel to axial direction. Fig. 10 indicates that

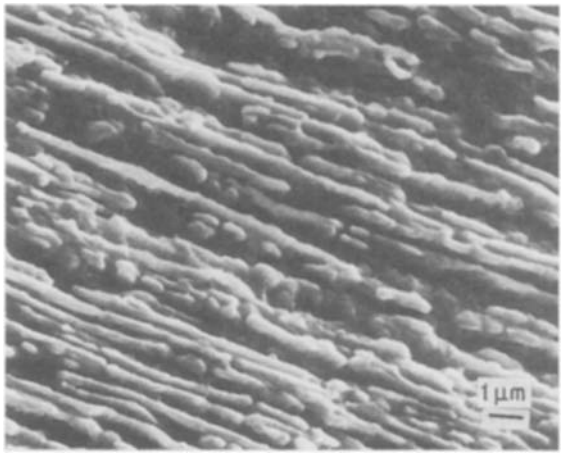

Figure 10 Oxide–metal interface in a pre-transition specimen with oxide layer parallel to axial direction of pressure tubing.

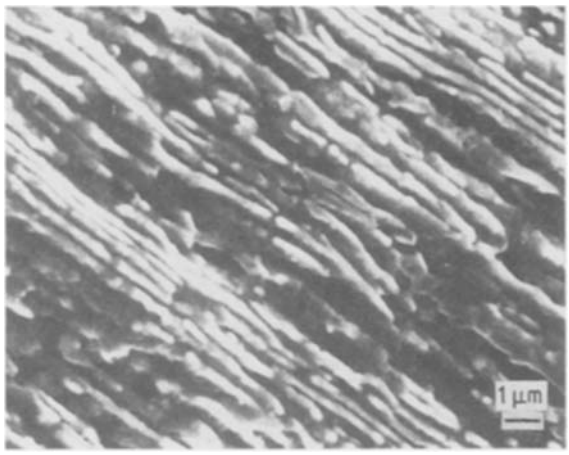

Figure 11 Oxide–metal interface in a post-transition specimen with oxide layer parallel to axial direction of pressure tubing.

there is a definite demarcation line between oxide and metal at the interface in pre-transition specimens. This results from the same corrosion rates on an identical specimen surface. Therefore, the oxide front formed during corrosion of a pre-transition specimen is located at a constant level (from the metal surface). From Fig. 11 it can be seen that the demarcation line between oxide and metal at the interface in post-transition specimens is not straight but is rather jagged. This is due to variations in the corrosion rates. Where there are the highest corrosion rates, there are 'fingers' of oxide that protrude from the general oxidation front. These high corrosion rates probably resulted from a greater surface area (of the faster corroding structure/phases) and the presence of a deformed layer of metal at the oxide–metal interface in the post-transition specimens [6].

4. Discussion

4.1. Effect of grain boundary structure and chemistry on corrosion of Zr–2.5Nb

The corrosion resistance of Zr–2.5Nb is known to be sensitive to the metallurgical history and the microstructure that is developed [7]. In the commercial pressure tubing a satisfactory corrosion resistance is obtained in tubing which is made by extrusion at 850 °C (in α-Zr + β-Zr region), cold-working and stress-relieving (autoclaving) at 400 °C for 24 h. After processing (extrusion + cold-working), Zr–2.5Nb pressure tubing contains elongated α-Zr grains and a grain-boundary network of metastable β-Zr that contains ~ 20 wt % niobium. Upon heating at 400 °C for 24 h or after corrosion for longer times at 300 °C (the reactor operating temperature) the metastable β-Zr will slowly decompose to an equilibrium structure consisting of α-Zr and β-Nb (~ 85% Nb). However, on the basis of the published TTT (temperature, time, transformation) diagrams for 12–25 wt % niobium alloys, the time required for complete decomposition (at 300 °C) to β-Nb could be several years [8] and several intermediate decomposition products can be found, including ω phase and β-enriched (intermediate in Nb content between β-Zr and β-Nb: enriched in Nb with respect to β-Zr).

The grain boundaries in cold-worked Zr–2.5Nb pressure tubing can thus contain β-Zr and its decomposition products together with impurities and other precipitates [9–11]. There are thus many kinds of boundaries formed between these phases. At the beginning of the corrosion process, oxidation should proceed rapidly along grain boundaries. The oxides formed at grain boundaries may be either the 'regular' ZrO_2 or oxides formed from oxidation of impurities. The grain boundaries formed between the oxides can become short-circuit paths for the diffusion of oxygen anions to the oxide–metal interface. At this time, oxidation at grain boundaries is faster than on the bulk α-Zr grains. If the rate of diffusion is high at the interface, it is possible for porosity to develop in the oxide in the vicinity of β-Zr filaments. It is also likely that short-circuit diffusion via flaws in oxide, which are formed during β-Zr oxidation, is another major route for anion diffusion. As will be discussed below, microcracking induced by transformation of ZrO_2 may also cause short-circuit diffusion.

Looking at other possible reasons for enhanced oxidation at the grain boundaries, it is noted that Dyment and co-workers [12, 13] found that Zr and Nb diffusion coefficients along the α/β Zr interface were three to four orders of magnitude higher than for bulk diffusion in the corresponding β-phase, and more than six orders higher than in the bulk α-phase. Although tracer studies have shown that zirconium oxidation occurs almost entirely by inward anion diffusion through the oxide to the oxide–metal interface, cation diffusion might become important at grain boundaries because of increasing diffusion coefficients. Also there is evidence that cation diffusion can become more important across an oxide–metal interface when the oxide is in compression [14].

4.2. Proposed mechanism for breakaway corrosion

As previously noted, zirconium and its alloys, oxidized in several environments, usually show two principal kinetic periods. There is an initial period in which the rate of oxidation decreases with time, followed by a second period in which there is an increase to a quasi-linear oxidation rate [15]. Cox [1, 2], on the basis of mercury porosimeter studies, explained the breakaway (i.e. transition in corrosion kinetics) by the development of networks of micropores in protective oxide films, induced by recrystallization of the oxide. An alternative mechanical detachment hypothesis is represented by Bradhurst and Heuer [3]. In this theory, breakaway occurs because of the mechanical detachment of the protective oxide film resulting from stresses in the oxide film.

Differences in the pore structures of the oxides formed on Zircaloy-2 and Zr–2.5Nb have been noted [1]. For Zircaloy-2, the evidence indicates that the pore network that develops in the post-transition oxidation regime penetrates to the oxide–metal interface, whereas for the Zr–2.5Nb alloy the evidence suggests that an impervious barrier layer of oxide persists to very high weight gains, although the outer

part of the oxide is porous. Cox [16] has suggested that the pores or microcracks in the oxides on Zircaloy-2 penetrate to a point very close to the oxide–metal interface, but that such a phenomenon does not occur in oxide films on Zr–2.5Nb.

In our recent TEM study of the oxide–metal interface formed during the aqueous corrosion of Zr–2.5Nb alloy, we showed that the oxide at the oxide–metal interface was tetragonal ZrO_2 rather than monoclinic ZrO_2 [17]. The retention of tetragonal ZrO_2 at the oxide–metal interface was attributed to the fine grain size of the ZrO_2 and the compressive stresses developed at the oxide–metal interface [17]. These compressive stresses result from the high Pilling–Bedworth ratio (1.56). According to the work of Whitney [18] and Kulcinski [19], tetragonal ZrO_2 can be retained at room temperature by applying pressures greater than 3700 MPa. The maximum average stress measured that can be retained at the interface increases with the strength of the metal substrate. Since Zr–2.5Nb alloy is one of the stronger zirconium alloys, this allows higher compressive stresses to be retained and more tetragonal ZrO_2 grains to be formed than in other Zr alloys. The compressive stress gradient through the thickness of black oxide films on Zircaloy-2 has been measured as 500 MPa μm^{-1} for a film thickness of 1.2 μm but decreased to 60 MPa μm^{-1} with the increase of thickness to 2.1 μm [20]. Given this steep stress gradient, the tetragonal ZrO_2 retained because of compressive stresses may only exist over a small distance. Once the compressive stresses has decreased below the critical value (3700 MPa), tetragonal ZrO_2 should transform to monoclinic ZrO_2 providing there are not other factors, such as small grain size or chemical stabilizers, which could also help retain the tetragonal structure. The $ZrO_2(t) \rightarrow ZrO_2(m)$ transformation can result in both microcracking and twinning [20]. This microcracking may also increase short-circuit diffusion and contribute to the increase in oxidation rate.

Based on the results of the SEM examination, and on other models and data in the literature, we present in Fig. 12 a qualitative picture of the processes occurring during the aqueous corrosion of Zr–2.5Nb. In the early stages, the oxide formed on metal surface is produced mainly from the oxidation of the grain-boundary phases, i.e., β-Zr and its decomposition products. The oxide formed from grain-boundary phases may be not dense enough to act as a barrier layer, especially the upper oxide layer (see Fig. 12), i.e. that furthest from the α-Zr/β-Zr interface. Oxidation of the α-Zr grains may form a dense protective oxide barrier at the oxide α-Zr interface: this oxide is predominantly tetragonal ZrO_2. The protective oxide layer is characterized by wave shape, i.e. it follows the contours of the α-Zr grain surfaces. The average weight gains of the specimen in groups A and B are 40 and 640 mg dm^{-2}, which correspond to oxide thickness of 2.7 and 43 μm, respectively. Comparing Figs 8 and 9, which show the oxide–metal interface in the pre- and post-transition regions, long ridges of oxides can be seen in the post-transition specimens. These oxide ridges can deform and eventually destroy the protective oxide barrier layer. When the pressure of the hydrogen gas which is accumulating gradually at the oxide–metal interface reaches a critical value, which is smaller in a post-transition specimen than in a pre-transition specimen, the protective oxide layers are broken. Because this deformation, and eventual destruction, of the protective oxide barrier layer is a gradual process as the specimen goes from the pre-transition to the post-transition stage, the change from parabolic to linear kinetics is also a gradual process.

5. Conclusions

Detailed SEM studies show that the oxidation of cold-worked Zr–2.5Nb pressure tubing in pressurized lithiated water at 300 °C proceeds first along grain

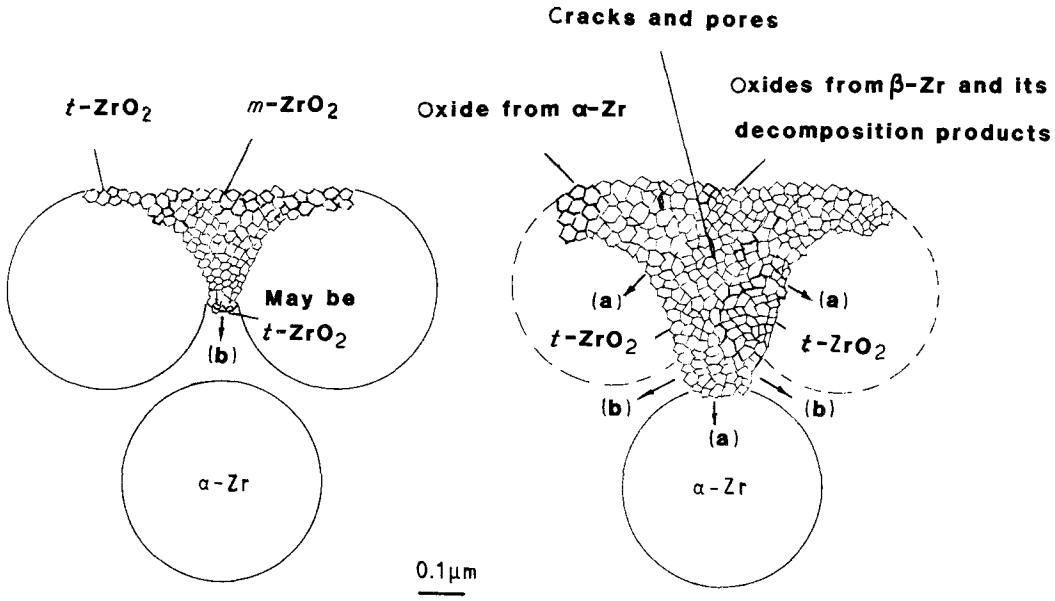

Figure 12 Schematic illustration of the processes occurring during the oxidation of Zr–2.5Nb in an aqueous environment. (a) corrosion on α-Zr; (b) boundary corrosion.

boundaries at which there are β-Zr and its decomposition products, and then continues on α-Zr grains. The oxides formed were mainly extended along grain boundaries, and were characterized by long filaments, which are composed of many fine ZrO_2 grains. Short-circuit diffusion at grain boundaries is mainly related to oxidation of grain-boundary phases, flaws arising from β-Zr filaments, and microcracking arising from phase transformation of ZrO_2.

When different sections of a given specimen are corroded under the same environmental conditions, different corrosion rates can result with sections containing a high area fraction of long grain boundaries having higher corrosion rates.

The long ridges of oxides, which are formed in the post-transition specimens, result in the destruction of the protective barrier layer, and hence an increase in the oxidation rate.

Acknowledgements

This work was supported by the Natural Sciences and Engineering Research Council of Canada (operating Grant A4391) and the CANDU Owners' Group (COG). One of the authors (Y. D.) acknowledges the scholarship provided by the Pao Yu-kong Foundation. Mr John W. Robinson assisted with the corrosion tests and with the SEM examinations.

References

1. B. COX, *J. Nucl. Mater.* **148** (1987) 332.
2. *Idem., ibid.* **29** (1969) 50.
3. D. H. BRADHURST and P. M. HEUER, *ibid.* **37** (1970) 35.
4. B. D. WARR, E. M. RASILE and A. M. BRENNENSTUHL, Presented at the IAEA Technical Committee Meeting on Fundamental Aspects of Corrosion of Zirconium-Base Alloys for Water Reactor Environments, Portland, Oregon, September 1989. Also published as COR-I-89-199, November 1989.
5. R. A. PLOC, *J. Nucl. Mater.* **99** (1981) 124.
6. T. AHMED and . L. H. KEYS, *J. Less-Common Metals* **39** (1975) 99.
7. V. F. URBANIC and R. W. GILBERT, Presented at the IAEA Technical Committee Meeting on Fundamental Aspects of Corrosion of Zirconium-Base Alloys for Water Reactor Environments, Portland, Oregon, September 1989.
8. R. F. HEHEMANN, *Can. Met. Quart.* **11** (1972) 201.
9. X. MENG and D. O. NORTHWOOD, in "Zirconium in the Nuclear Industry", Proceedings of the Eighth International Symposium, ASTM STP 1023, edited by L. F. P. Van Swam and C. M. Eucken (American Society for Testing and Materials, Philadelphia, 1989) p. 478.
10. O. T. WOO, G. J. C. CARPENTER, J. A. SAWICKI and S. R. MACEWEN, *J. Nucl. Mater.* **172** (1990) 71.
11. C. P. LUO and G. C. WEATHERLY, *Metall. Trans. A* **19A** (1988) 1153.
12. M. J. IRIBARREN and F. DYMENT, *J. Nucl. Mater.* **161** (1989) 148.
13. R. PIOTRKOWSKI and F. DYMENT, *ibid.* **137** (1986) 94.
14. A. ATKINSON, *Rev. Mod. Phys.* **57** (1985) 437.
15. B. COX, in Proceedings of the Electrochemical Society Fall Meeting, 1981.
16. *Idem.*, Report AECL-9382, Atomic Energy of Canada Ltd., (1987).
17. Y. DING and D. O. NORTHWOOD, Presented at the 23rd Annual Meeting of the International Metallographic Society, Cincinnati, Ohio, U.S.A., July 1990. To be published in *Microstructural Science* **19**.
18. E. D. WHITNEY, *J. Amer. Ceram. Soc.* **45** (1962) 612.
19. G. L. KULCINSKI, *ibid.* **51** (1968) 582.
20. ZHOU BANG-XIN, "Zirconium in the Nuclear Industry", Proceedings of the Eighth International Symposium, ASTM STP 1023, edited by L. F. P. Van Swam and C. M. Eucken (American Society for Testing and Materials, Philadelphia, 1989) p. 360.
21. F. F. LANGE, *J. Mater. Sci.* **17** (1982) 225.

Received 19 October 1990
and accepted 28 February 1991